JGR Atmospheres

Special Section:
Atmospheric Rivers: Intersection of Weather and Climate

Key Points:
- Sub-tropical surface evaporation is linked to East Antarctic precipitation via long-range atmospheric moisture transport
- Long-range poleward moisture transport is enhanced by synoptic-scale slantwise isentropic ascent and by embedded explosive mesoscale cyclogenesis
- The primary moisture source for Antarctic precipitation is located over the sub-tropics

Supporting Information:
Supporting Information may be found in the online version of this article.

Correspondence to:
A. Terpstra,
annick.terpstra@uib.no

Linking Sub-Tropical Evaporation and Extreme Precipitation Over East Antarctica: An Atmospheric River Case Study

Annick Terpstra[1,2] , Irina V. Gorodetskaya[2], and Harald Sodemann[1]

[1]Geophysical Institute, University of Bergen, Norway and Bjerknes Center for Climate Research, Bergen, Norway, [2]Department of Physics, CESAM-Centre for Environmental and Marine Studies, University of Aveiro, Aveiro, Portugal

Abstract We investigate an intense snowfall event between 15 and 18 February 2011 over the East Antarctic coastal region which contributed to roughly 24% of the annual snow accumulation. The event was previously associated with an atmospheric river, and here we use both Eulerian and Lagrangian analysis to gain an understanding of the processes contributing to the atmospheric river signature. The planetary-scale configuration during the event consisted of a persistent blocking situation resulting in a sustained meridional flow from the sub-tropics to the Antarctic ice sheet between 20 and 50°E. Within this configuration, synoptic-scale cyclogenesis contributed to slantwise ascent of moisture loaded air parcels toward Antarctica. Landfall of this cyclone's warm sector coincided with the onset of Antarctic precipitation. Subsequently, a secondary cyclone developed along a pre-existing baroclinic zone. The rapid intensification and propagation speed of this mesoscale cyclone alongside the warm, moist air mass resulted in strong moisture flux convergence ahead of the cyclone, providing additional poleward moisture transport. The poleward progression of warm moist air and a corresponding decrease of sea-surface temperatures implied downward surface sensible and latent heat fluxes throughout the region of intense poleward moisture, roughly between 40 and 60°S. Hence, moisture uptake via surface evaporation was suppressed between the sub-tropics and the polar continent, favoring long-range transport. Identification of the surface moisture uptake region by tracing changes in moisture in air parcels confirmed the limited uptake of moisture during the poleward transport in this case study, with the primary moisture source for Antarctic precipitation located in the sub-tropics.

1. Introduction

During the last decades the Antarctic ice sheet encountered a net loss in mass (Rignot et al., 2019). However, the spatial distribution of this overall ice-sheet mass loss exhibits stark contrasts, with reductions in the ice-sheet mass over West Antarctica being partly counterbalanced by increases in mass over East Antarctica (Andrew et al., 2018; King et al., 2012; Shepard et al., 2012). Boening et al. (2012) indicated that the limited mass loss over East Antarctica, in particular between 2009 and 2011, could be attributed to enhanced precipitation over the region. Moreover, recent observations show that extreme precipitation events are the dominant contributors to local snow-accumulation in this region (Boening et al., 2012; Gorodetskaya et al, 2014, 2015; Souverijns et al., 2018). Precipitation, predominantly as snowfall, is the only significant source term for the mass balance of the Antarctic ice-sheet (Bromwich, 1988). The majority of continental Antarctic precipitation is predestined for a long residency as part of the Antarctic ice-sheet and thus constitutes the content of ice cores, our prime source of long-term climate information over the region (Landais et al., 2017; Schlosser et al., 2017; Stenni et al., 2016). While a significant fraction of the total precipitation over Antarctica, 35% over the interior increasing to 50%–70% toward coastal regions, is attributable to extreme (>90th percentile) precipitation days (Turner et al., 2019). Thus, to contextualize snow-accumulation over Antarctica, including the role of the Antarctic ice-sheet in the global hydrological cycle during the present and future climate, insight into the drivers and processes responsible for these extreme precipitation events is instrumental.

By employing Lagrangian analysis Sodemann and Stohl (2009) identified moisture source regions for Antarctic precipitation. In that study, contributions from surface evaporation to precipitation over East Antarctica exhibit a maximum over the Southern Ocean around 40°S and decreases poleward. Furthermore,

the moisture source region for precipitation over East Antarctica is located westward of the precipitation location. Subsequent studies employing Lagrangian analysis confirmed the moisture source maximum along this latitude band for the EPICA ice-core site in East Antarctica (Drumond et al., 2016). The surface moisture source maximum centered around 40°S is collocated with the climatological latitude band of a strong meridional sea surface temperature (SST) gradient, which marks a latitudinal separation between regions of relatively weak and strong surface evaporation. Poleward of 40°S precipitation is larger than surface evaporation, resulting in a net freshwater input from the atmosphere over the Southern Ocean, with 60%–75% of the precipitation in this region attributable to fronts and cyclones (Papritz et al., 2013). The distinct gap of several thousand kilometers between the moisture origin maximum and precipitation location underscores the role of long-distance meridional moisture transport in the atmosphere for precipitation over East Antarctica.

Zhu and Newell (1998) pointed out that meridional moisture transport in the lower troposphere is predominantly organized in filamentary structures, a phenomena commonly referred to as an "Atmospheric River" (AR). Elongated structures of intense moisture transport are often embedded in the warm sector of an extra-tropical cyclone, where the process of cyclogenesis results in isentropic upgliding of warm moist air and local moisture convergence along the advancing cold front, both contributing to high values of vertically integrated water vapor transport (IVT) (e.g., Cordeira et al., 2013). Clusters of cyclones can maintain and extend the elongated signature of ARs, where enhanced surface evaporation in the previous cyclone's cold sector contributes to the moisture available for subsequent cyclones (Cordeira et al., 2013; Sodemann & Stohl, 2013). ARs are frequently associated with intense coastal precipitation (e.g., Gimeno et al., 2016). They supply the necessary moisture for intense and sustained precipitation with interactions between the flow and orography resulting in adiabatic cooling and local moisture convergence triggering precipitation (e.g., Ralph et al., 2010). The high-latitude regions are no exception, and AR signatures have been linked to intense precipitation events along the coastal region in East Antarctica (Gorodetskaya et al., 2014; Kurita et al., 2016). However, identification of anomalous tropospheric moisture transport prior to and during precipitation events provides only a limited understanding of the contribution to local precipitation. By combining observations and reanalysis data, Welker et al. (2014) stressed that intense precipitation events over East Antarctica are generally associated with above average IVT values, but that large IVT values do not necessarily result in intense precipitation. Their study further illustrates that the magnitude of IVT is secondary to the directionality of IVT, with directions perpendicular to the orography most favorable for precipitation formation. Thus, identification of the atmospheric pathways producing these favorable high IVT signatures potentially contributes to our understanding in the processes associated with extreme precipitation events over East Antarctica.

Poleward moisture transport requires, besides the atmospheric moisture content, a meridional orientated flow direction. Spatially and temporally sustained meridional flow conditions are associated with planetary scale waves, that is, meandering of the mean polar front, with atmospheric blocking events over the Southern Ocean in the East Antarctic regions generally lasting between 5 and 6 days (Mendes et al., 2008). The relevance of the large-scale atmospheric configuration for sustained meridional moisture transport is demonstrated by ARs reaching the Antarctic continent coinciding with blocking conditions (Wille et al., 2019), and several extreme precipitation cases over East Antarctica aided by blocking conditions (Gorodetskaya et al., 2014; Hirasawa et al., 2013; Schlosser et al., 2010).

The majority of meridional moisture transport over the Southern Ocean is associated with transient eddies (Tietäväinen & Vihma, 2008), though the dominant propagation direction for most of these cyclones is eastward (Uotila et al., 2013) and thus they are unlikely to contribute significantly to precipitation over the Antarctic continent. Sinclair and Dacre (2018) considered the meridional moisture flux associated with poleward propagating cyclones over the Southern Ocean. They found that cyclones with genesis locations further equator-ward exhibited larger meridional moisture fluxes than cyclones that have their genesis location closer to the Antarctic continent. Hence, in line with the maximum of moisture sources for Antarctic precipitation around 40°S, atmospheric loading of moisture via oceanic evaporation has smaller amplitudes closer to the continent. Yet, the strongest meridional moisture fluxes were associated with rapidly poleward propagating open frontal waves, akin to secondary cyclogenesis. Cyclones attain poleward directionality due to the effects of upper level vorticity gradients and diabatic heating (Tamarin & Kaspi, 2016), yet their

main translation speed and direction are closely tied to the background flow with blocking conditions favoring poleward propagation (Booth et al., 2017).

In this study we analyze moisture transport and sources that contributed to an extreme precipitation event between 15 and 18 February 2011 over East Antarctica. Gorodetskaya et al. (2014) first identified this same event as an AR and showed its remarkable contribution to the local surface mass balance. Here we further explore the atmospheric evolution of the event, assess the role of air-sea interactions, and elucidate the synoptic and mesoscale contributions to long-range moisture transport. We start with briefly describing the spatial and temporal evolution of the continental precipitation and use local precipitation observations to assess the ability of reanalysis data to resolve the event (Section 3.1). Followed by a Eulerian description of the associated moisture transport toward Antarctica separating between synoptic (Section 3.2.1) and sub-synoptic scales (Section 3.2.2), which we complement with a Lagrangian approach (Section 3.3). Finally we pinpoint the sub-tropical oceanic evaporation regions that contributed to the continental precipitation (Section 3.3.2) by tracing moisture changes in airparcels before arriving at the precipitation region.

2. Data and Methods

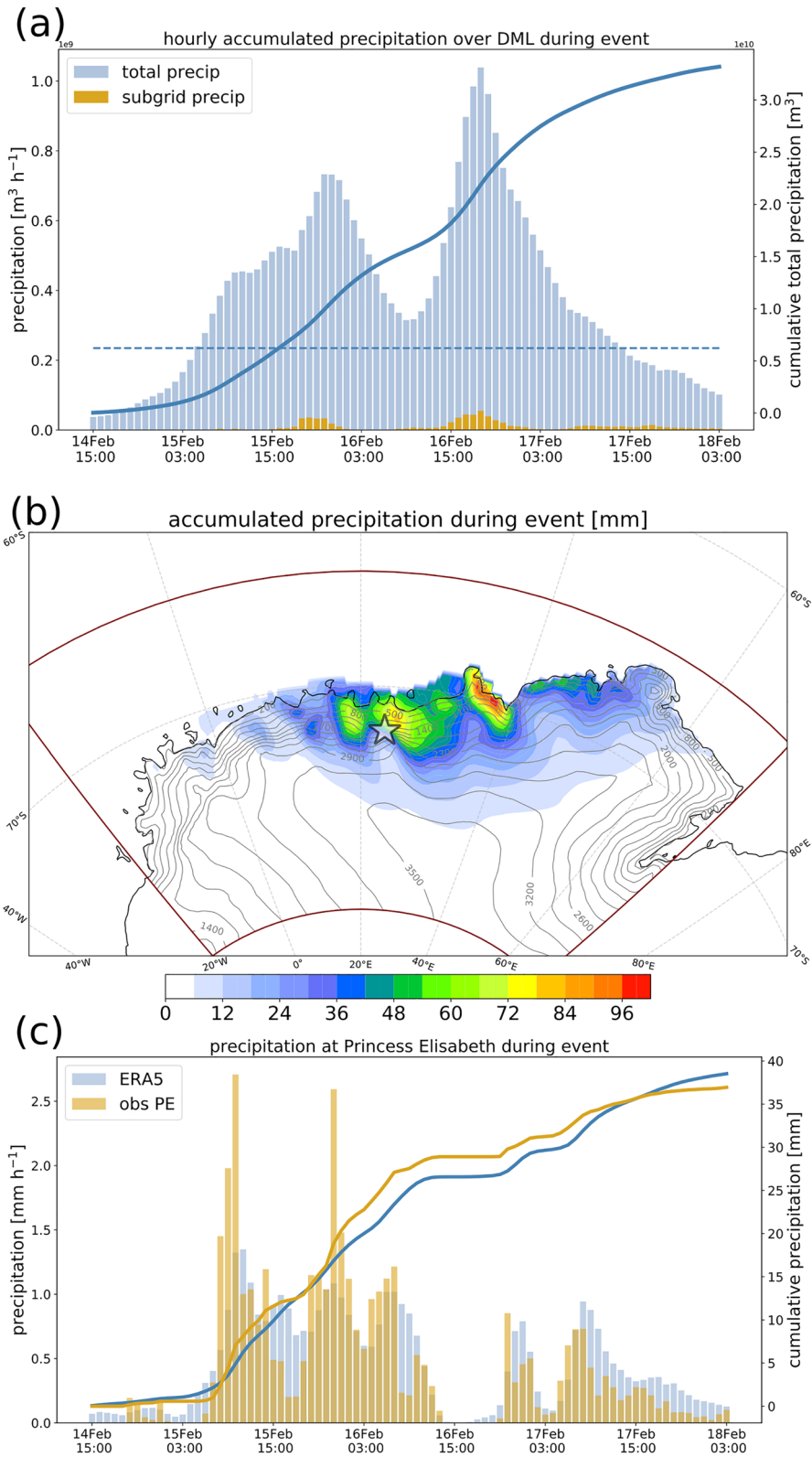### 2.1. Reanalysis, Trajectories, and Feature Detection

For the analysis we use the latest reanalysis product of the European Centre for Medium Range Weather Forecast (ECMWF). ERA5 (Hersbach et al., 2020) is based on 4D-Var data-assimilation in ECMWF's Integrated Forecast System (IFS), and provides a best estimate of the state of the atmosphere by combining observations and numerical modeling. We used ERA5's high resolution realization (HRES) interpolated to a horizontal resolution of 0.25° (≈28 km) with hourly temporal resolution.

Kinematic backward trajectories are initiated every 3 hours for the period 15–18 February 2011 using the LAGrangian ANalysis TOol (LAGRANTO, Sprenger & Wernli, 2015), and are based on ERA5 data interpolated to 0.5° resolution with 3-hourly temporal resolution. The 10-day backward trajectories are initialized on an equidistant 30 km grid at pressure-intervals of 25 hPa between 1,000 and 750 hPa and 50 hPa intervals between 750 and 300 hPa over the continent in the region bounded by 65°S–76°S and 7°W–65°E. This region envelops the spatial area of the precipitation associated with the event.

We apply automatic detection of low-level cold and warm fronts based on Hewson (1998) and Jenkner et al. (2010) to identify elongated structures of horizontal gradients $>3 \times 10^{-5}$ K m^{-1} in the potential temperature at 850 hPa. Cyclone labels, L_1 and $L_{S1..S3}$, are for guidance and identified by manually inspecting hourly meteorological fields.

2.2. Precipitation Observations

Precipitation measurements are from the cloud-precipitation-meteorological observatory at the Belgian Princess Elisabeth (PE) research station in East Antarctica (Gorodetskaya et al., 2015). The PE observatory (71°57′S, 23°21′E, see Figure 1c) is located in the escarpment zone (≈180 km inland) of Dronning Maud Land (DML), just north of the Sør Rondane mountain chain at an elevation of 1,392 m above mean sea level. Precipitation rates are derived from the precipitation radar (Metek's Micro Rain Radar, MRR-2) installed at PE station in February 2010 (Gorodetskaya et al., 2015). This is a frequency-modulated continuous-wave vertically profiling Doppler radar transmitting at 24 GHz frequency. The radar effective reflectivity (Z), Doppler velocity and spectral width are calculated from the raw Doppler spectra measurements using the algorithm of Maahn and Kollias (2012). The MRR-2 setup at PE provides precipitation profiles at 60 s temporal resolution up to 3,000 m above ground level with 100 m vertical resolution. The first useful range near the ground is at 400 m, which is used to calculate precipitation reaching the surface (Gorodetskaya et al., 2015) by converting the associated effective reflectivity (Z) to snowfall rates (S) using various Z-S relationships for dry snow (Grazioli et al., 2017; Kulie & Bennartz, 2009; Matrosov, 2007; Souverijns et al., 2017). To compare the observations with ERA5, we aggregate the derived snowfall rates over the previous hour, such that the observations are in agreement with ERA5 cumulative precipitation fields.

(a) hourly accumulated precipitation over DML during event

(b) accumulated precipitation during event [mm]

(c) precipitation at Princess Elisabeth during event

2.3. Identification of Moisture-Source Regions

Moisture sources are diagnosed from the backward trajectories using the software tool WaterSip (Sodemann, 2020; Sodemann et al., 2008). The Watersip method evaluates changes in specific humidity along the backward trajectories to identify periods of moisture uptake and loss in the traced air masses. If specific humidity increases by more than 0.1 g kg^{-1} in a 3 h period, a moisture source is identified. The method distinguishes between uptake events within a proximity of the surface that indicates a direct contribution from surface evaporation, and more indirect cases of moisture detrainment from the boundary layer. Evaluating the entire trajectory with this moisture accounting method provides a quantitative estimate of the entire fraction of moisture at the time of precipitation which can be related to its sources. The precipitation itself is estimated from the specific humidity decrease at the latest time step of the backward trajectories, and converted to precipitation in units of mm 3 h^{-1} by integrating over the regular x-y-p grid. Recently, in an evaluation of the WaterSip method, Sodemann (2020) pointed out that the results of the method are likely biased toward the more substantial moisture uptakes (contributing to the humidity of air masses on time scales of up to 10 days) due to applied thresholds and the limitations of trajectory calculations, while weaker events of mixing with humidity from surrounding or down welling air masses are under-estimated. Yet, evaporation contribution patterns identified by the WaterSip method show striking similarity with conceptually similar Eulerian diagnostics of strong large-scale ocean evaporation events (Aemisegger & Papritz, 2018), including the Southern Ocean regions.

3. Results

In this study we examine the atmospheric pathway associated with an extreme precipitation event over East Antarctica. Prior to and during the precipitation event an elongated structure with anomalous high values of IVT extended from the sub-tropics to the Antarctic continent, as such the event was previously identified as an atmospheric river (Gorodetskaya et al., 2014). Here we aim to gain some understanding of the atmospheric processes contributing to this high IVT signature. We focus in particular on long-range moisture transport and the interplay between atmospheric scales (planetary to mesoscale) and air-sea interactions therein. The event lasted about 4 days (between 15 and 18 February 2011) and contributed to roughly 24% of the total yearly accumulation observed at Princess Elisabeth Station (Gorodetskaya et al., 2014). Thus within a relative short period this event had a profound impact on the local snow-accumulation, underlining the relevance of these types of events for the total ice-sheet mass balance (Boening et al., 2012; King et al., 2012; Lenaerts et al., 2013).

3.1. Precipitation

Based on ERA5-data, the event was associated with some of the largest peak values in precipitation over the DML-region in 2011 and exhibited sustained precipitation amounts in excess of the 95th percentile for 2011 for ≈2.5 days (dashed line, Figure 1a). Virtually all precipitation in ERA5 resulted from large-scale (resolved) processes (Figure 1a), indicating the dominant role of non-convective processes in precipitation formation during the event over the Antarctic ice-sheet. The event comprised two phases of amplified precipitation. The initial onset of enhanced precipitation was around 15 February 03:00 UTC and culminates about 20 h later in a peak of precipitation (15 February 23:00 UTC), thereafter the precipitation decreases. Roughly 14 h later the precipitation increased again (16 February 13:00 UTC), peaking for the second time 7 h later (16 February 20:00 UTC), followed by a longer lasting decay (approximately 22 h) marking the end of the event. Note that both stages contribute approximately equally to the total precipitation during the event, as is evident from the cumulative precipitation (solid line, Figure 1a).

Figure 1. (a) Time-series of hourly accumulated total precipitation (blue bars) and unresolved precipitation (yellow bars) over the DML-region during the event (units: m^3 h^{-1}), corresponding cumulative total precipitation (blue, units: m^3), and the 95th percentile for hourly precipitation during 2011 (dashed line). (b) Spatial distribution of the accumulated total precipitation during the event (shading, units: mm) and orography (lines, units: m) over the DML-region. The box indicates the bounds for the DML-region (65°S–80°S, 20°W–70°E) and the location of Princess Elisabeth (71.95°S, 23.35°E) is marked with a star. (c) Precipitation at Princess Elisabeth station during the event for the nearest grid-box in ERA5 (blue bars), and derived from MRR measurements at the station (yellow bars, units: mm h^{-1}), and corresponding cumulative precipitation (blue and yellow line, respectively, units: mm). DML, Dronning Maud Land; MRR, Metek's Micro Rain Radar.

The prominent role of orography in the formation of precipitation is evident from the spatial distribution of the total accumulated precipitation during the event. The majority of the precipitation is confined to the DML coastal region, with peak values (up to 100 mm) located in the proximity of steep orography, that is, north and east of PE and west of the Lützow-Holm Bay (Figure 1b).

To verify the representation of the event in ERA5 we compared the precipitation for the nearest grid-point in ERA5 with MRR observations made at PE during the event (Figure 1c). The magnitude of precipitation estimates at PE are comparable to ERA5 accumulated precipitation fields when using the Z-S relationship based on Matrosov (2007) (Figure 1c). Notice however that absolute values of precipitation estimates derived from MRR observations are rather sensitive to the choices of the Z-S relation which depends on snow microphysical properties. For example, hourly accumulated peak values during the event based on Souverijns et al. (2017) are around 7 mm whereas peak precipitation estimates based on Grazioli et al. (2017) at a similar point in time are just over 2 mm, more than a threefold difference in magnitude. However, these choices primarily affect the magnitude of the precipitation as for each Z-S relation the estimated precipitation rates are proportional to the observed effective reflectivity. Hence, the temporal pattern of observed precipitation is not affected by the choice of the Z-S relationship, while assuming that snow microphysical properties do not differ significantly over space and time during the event.

The temporal evolution of the precipitation over PE is rather similar for the observation and ERA5. During the first phase of the event (roughly between 15 February 06:00 and 16 February 12:00) precipitation is present in both the observations and ERA5, with the precipitation in ERA5 showing a smoother evolution than the observations. As PE is located on the western side of the precipitation event, the first peak in precipitation has a stronger amplitude than the second peak, though also the second peak is clearly present in both ERA5 and the observations. Overall the temporal match between observation and ERA5 indicates that ERA5 captured the timing of the precipitation during the event, providing confidence that the atmospheric evolution associated with the event is sufficiently represented in the ERA5.

3.2. Eulerian Perspective

In this section we use a Eulerian perspective to describe the atmospheric structure, in particular the distribution of water vapor and associated moisture transport, during the onset of both precipitation peaks. We show that the initial onset of continental precipitation is associated with the landfall of the warm sector of a synoptic-scale cyclone, whereas the second peak is associated with the landfall of a secondary cyclone that developed along the persistent frontal zone of the main cyclone.

3.2.1. Synoptic-Scale Cyclogenesis

The atmospheric configuration prior to the onset of precipitation is characterized by a relatively steady trough located to the west of the precipitation region (Figure 2 and Figure S1). Upper-level conditions resemble anticyclonic wave breaking several days prior to the precipitation event, with undulations along the zonally directed part of the wave resulting in several smaller satellite cyclones accompanying the trough's main synoptic-scale cyclone (L_1, Figures 2a–2c). One of these mesoscale cyclones (L_{S1}) merges with the main cyclone, whereafter the ridge extends poleward, thereby introducing a region with poleward orientated flow throughout the entire depth of the troposphere on the upstream side of the ridge (Figures 2d–2f). Note the presence of tropical cyclone "Bingiza" over Madagascar, which potentially contributed to the intensification of the ridge. Upstream of the region dominated by this meridional flow a persistent high-pressure system and cut-off low are present during the event (Figures 2e and 2f and Figure S1). These conditions are often associated with atmospheric blocking (e.g., Woolings et al., 2018) and contributed to maintain the meridional flow beyond typical synoptic time-scales.

Prior to the ridge-building several regions of enhanced IVT associated with the mesoscale cyclones and zonally orientated flow are located between 35° and 45°S (Figures 2a and 2b). During the ridge-building some of these regions aggregate into the elongated region of strong IVT in the warm sector of the mature cyclone, that is, on the warm side of the cold-front (Figures 2c–2f). As the cyclone's warm sector translates toward Antarctica and the ridge amplifies (Figures 2d–2f), the band of high moisture transport becomes more meridionally orientated, eventually impinging on the Antarctic coastal region (Figure 2f). The onset
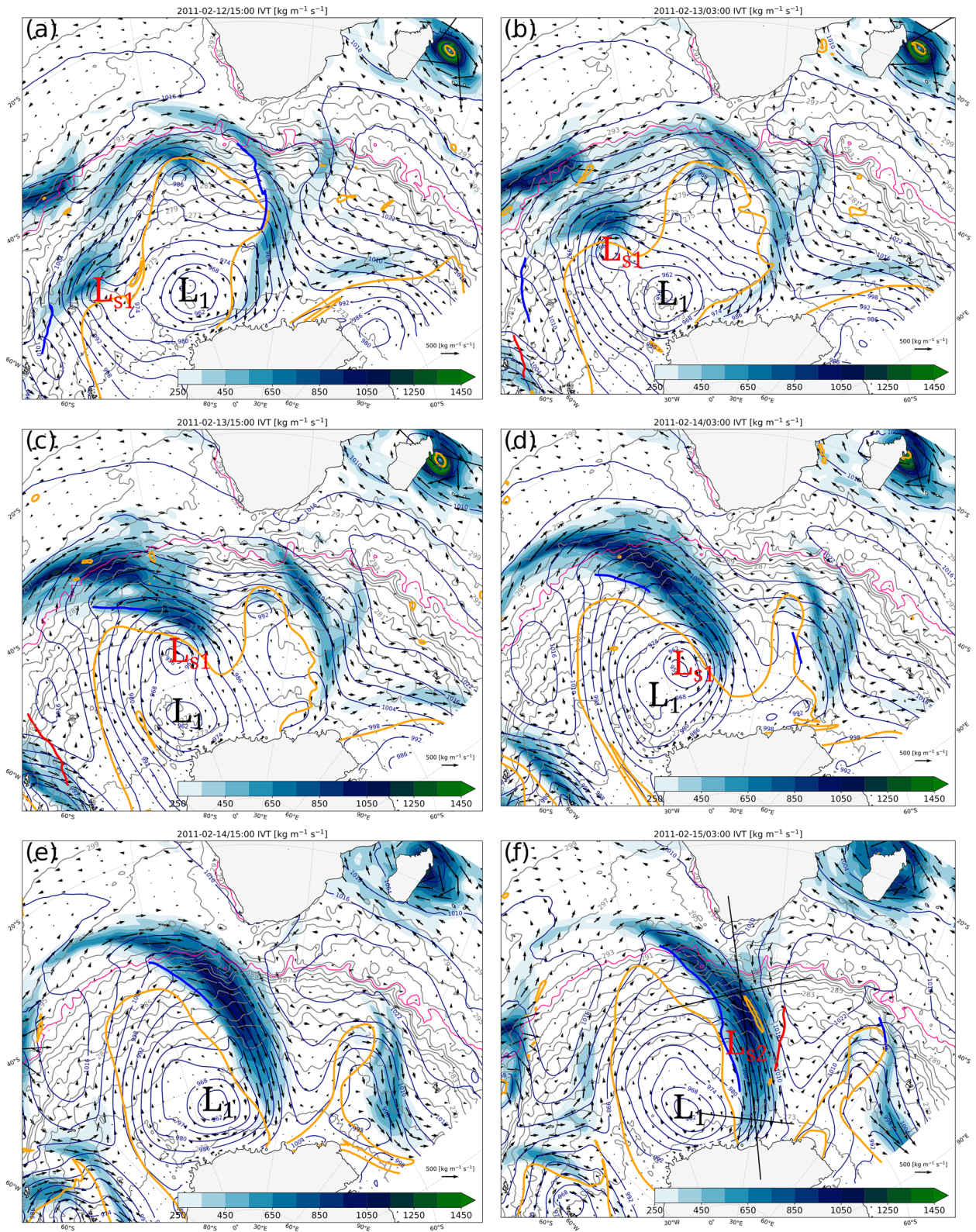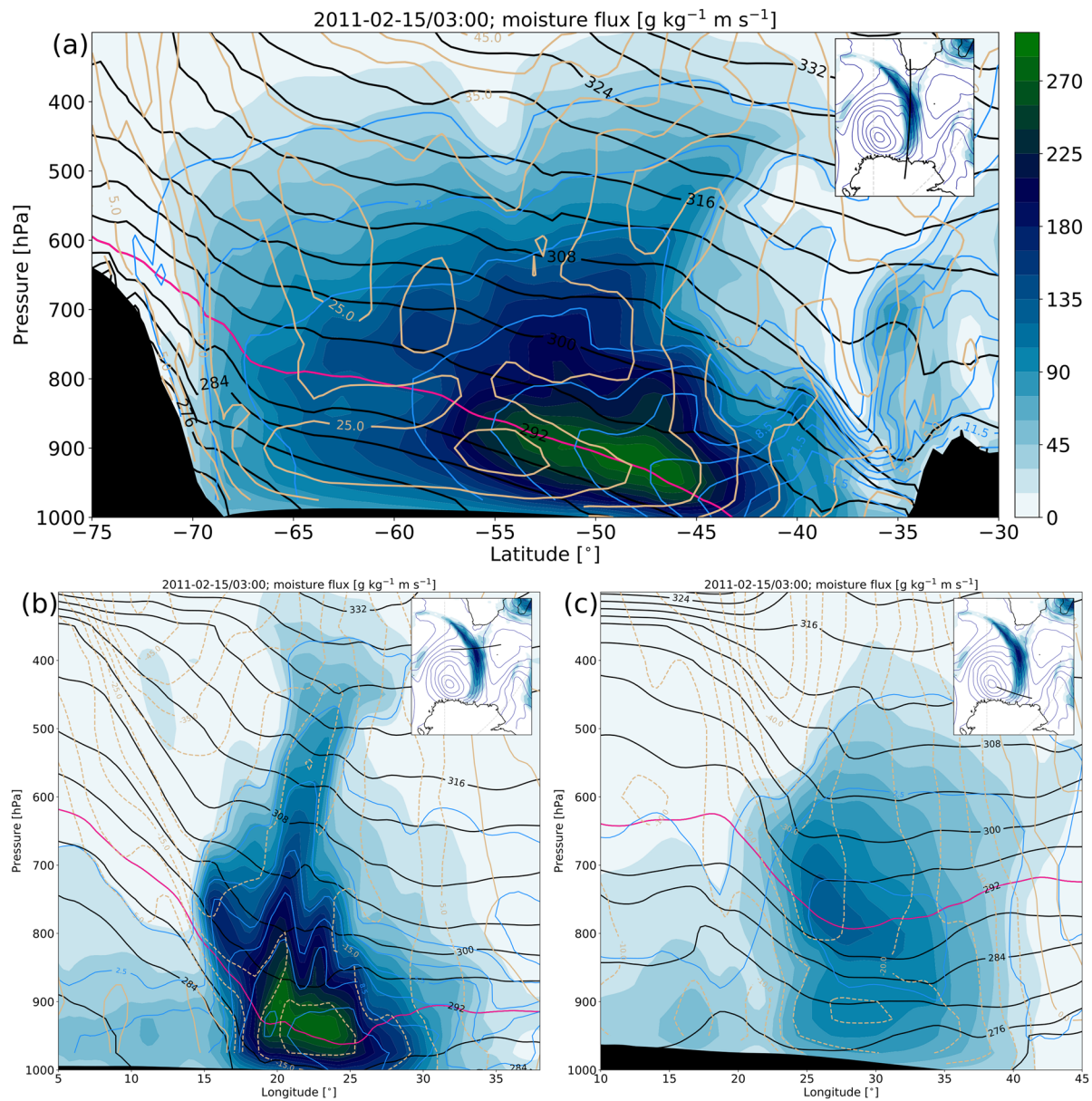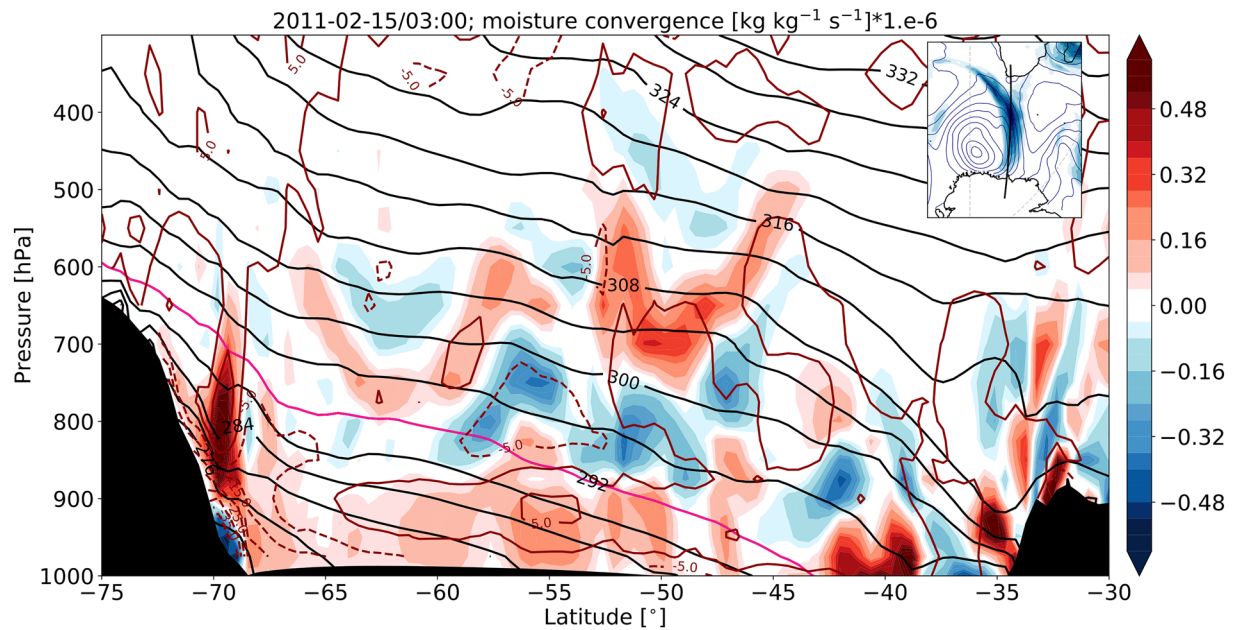
Figure 3. Vertical cross-section through the warm sector of the cyclone, showing moisture flux (shading, units: g kg m s^{-1}), potential temperature (black lines, units: K, pink-line = 292 K), specific humidity (blue lines, contour interval: 1.5 g kg^{-1}) and (a) along cross-section wind speed and (b, c) orthogonal wind speed (tan lines, negative dashed, contour interval: 5 m s^{-1}). Regions below the surface pressure are masked (black). The start and end point for the longitude of the cross-section in (a) are 20°E and 40°E, and for the latitude of the cross-section in (b) 42°S and 48°S, and both at 65°S for (c). The insert shows the location of the respective cross-section (black line) relative to the sea level pressure (lines) and vertically integrated moisture transport (shading), see also Figure 2f.

of precipitation over East Antarctica coincides with the moisture loaded warm sector, and thus the region of strong moisture transport, reaching the coastal zone of East Antarctica (Figure 2f).

Vertical cross-sections through the warm-sector at the onset of precipitation (15 February 03:00 UTC) provide some insights in the associated moisture transport toward East Antarctica (Figure 3). The maximum

Figure 2. Overview of the temporal evolution prior to the first precipitation onset (every 12 h, timestamps in UTC as per title), showing vertically integrated vapor transport (shading and arrows, units: kg m^{-1} s^{-1}), sea level pressure (blue lines, units: hPa), sea surface temperature (gray lines, units: K, pink line: SST = 292 K). Thick red and blue lines indicate low-level warm and cold fronts respectively, and the upper level configuration is depicted by the orange line representing 2PVU at 315 K. The main cyclone is marked as L$_1$, the secondary cyclones as L$_{S1}$ and L$_{S2}$, and the location of the vertical cross-sections in Figures 3 and 4 are indicated with lines on f). SST, sea surface temperature.

Figure 4. Vertical cross-section through the warm sector of the cyclone, displaying moisture convergence (shading, units: kg kg^{-1} s^{-1}), along-cross-section ageostrophic component of the velocity (indigo, units: m s^{-1}, negative dashed), and potential temperature (black lines, units: K, pink-line = 292 K). The insert shows the location of the cross-section (black line) relative to the sea level pressure (lines) and vertically integrated moisture transport (shading), see also Figure 2f.

of horizontal moisture transport in the vertical is found in the warm sector of the cyclone and roughly coincides with the 292 K isentrope. This isentrope intersects with the surface between 40° and 45°S (in a region with similar SSTs) and increases poleward in height from sea-level to around 800 hPa upon reaching the Antarctic coast, whereafter the isentropic steepness increases due to interaction with the steep topography of Antarctica. Relatively high values of moisture are found throughout the depth of the troposphere in the warm sector region, with narrow plumes at the northern end of the warm sector indicating some local convection (Figure 3b), whereas closer to Antarctica the distribution of moisture lacks these deep narrow plumes of moisture (Figure 3c). Jointly with the maximum of moisture transport, the vertical distribution of moisture (specific humidity) in the warm sector peaks also roughly around the 292 K isentrope. The wind-field exhibits poleward flow through the entire depth of the troposphere, with an upper level jet (≈400 hPa) to the west of a clearly distinctive low-level jet (enhanced wind speeds below 850 hPa) on the warm side of the cold front (Figures 3a and 3b). This low-level jet is primarily an ageostrophic feature associated with low-level horizontal convergence on the warm side of the cold front, and consequently amplifies low-level horizontal moisture convergence in the region of the low-level jet (Figure 4). The geostrophic flow does not exhibit a localized acceleration at the height of the LLJ (not shown).

Notice that toward Antarctica the height of the maximum wind speed associated with the low-level jet remains below 900 hPa. Thus the low-level jet region does not coincide with the local moisture maximum, nor with the local moisture transport maximum, but rather resides in a drier atmosphere below the local moisture maximum. This is clearly visible when comparing vertical cross-sections perpendicular to the warm sector. In the northern cross-section (Figure 3b), the 292 K isentrope, the maximum of specific humidity and low-level wind-maximum coincide around 950 hPa, thus establishing the maximum moisture transport at this level. In the southern cross-section (Figure 3c) the maximum of specific humidity (≈800 hPa) is above the low-level jet (≈900 hPa), yet the maximum of moisture transport is still found roughly around the 292 K isentropic. Thus the highest absolute values of moisture reaching the coastal zone of Antarctica are not at the height of the low-level jet, but located at slightly higher levels during the precipitation onset over East Antarctica.

Next we will consider the mismatch between the height of the moisture transport maximum and the low-level jet. The increased elevation toward Antarctica of the moisture transport maximum is in agreement with
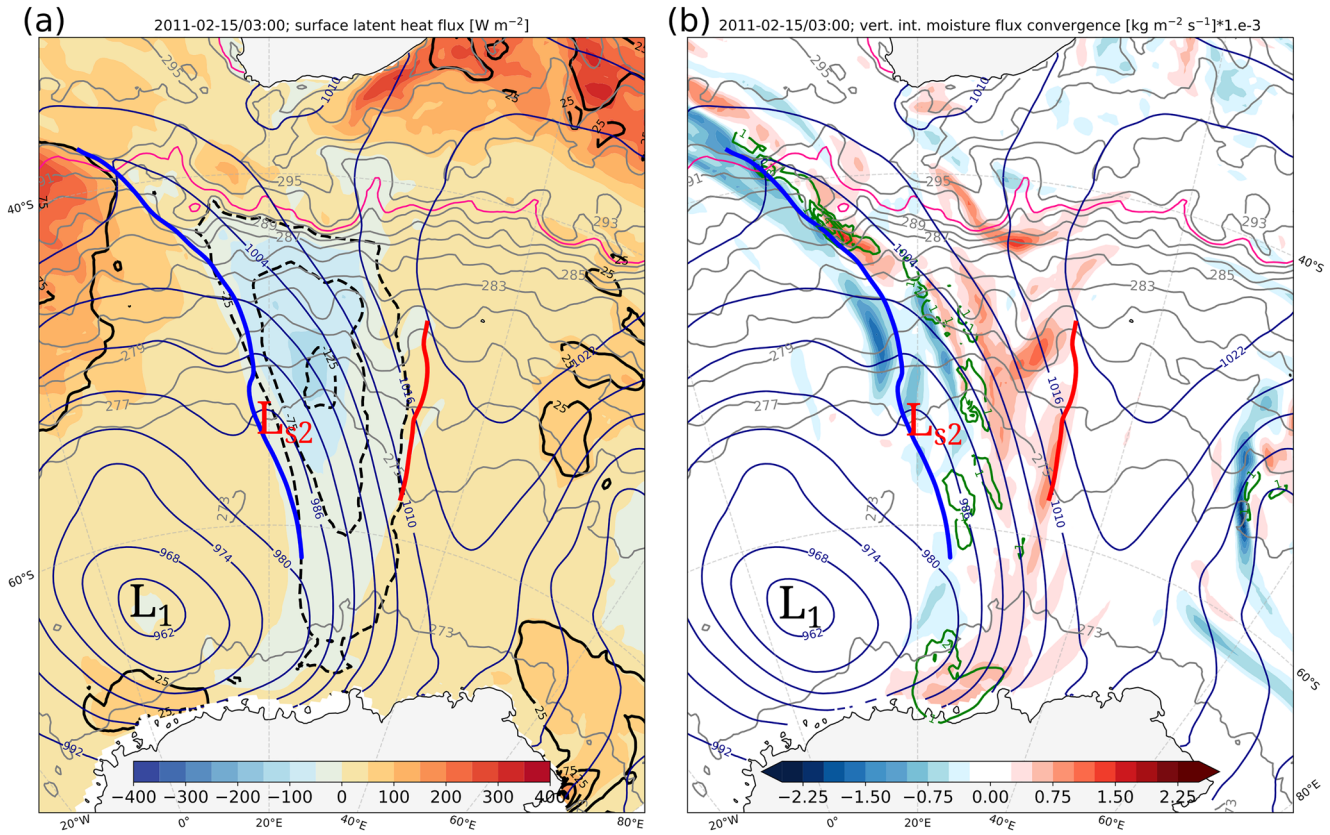
Figure 5. (a) Surface latent heat flux (shading, units: W m^{-2}) and surface sensible heat flux (black lines, negative dashed (downward), units: W m^{-2}). (b) Vertically integrated moisture flux convergence (shading, units: kg m^{-2} s^{-1}) and total precipitation (green, contour interval: 1 mm). Sea-level pressure (blue lines, units: hPa) and sea surface temperature (gray lines, units: K, pink-line: SST = 292 K). Thick red and blue lines indicate low-level warm and cold fronts respectively, the main cyclone is marked as L_1, and the secondary cyclone as L_{S2}. SST, sea surface temperature.

the warm-conveyor belt concept (WCB) (Madonna et al., 2014, e.g.,) in which cyclogenesis directs warm moist air upward along isentropic surfaces in the warm sector of a cyclone. The moisture loaded air-parcels ascent along moist isentropic surfaces, which are slightly steeper in the warm sector than isentropic surfaces (not shown), whereafter the air-parcel is only indirectly influenced by air-sea interactions as it detaches from the surface with increased height. As the warm sector progresses poleward it experiences colder underlying SSTs (Figure 5a). Roughly poleward of SST = 292 K, coinciding with a relative strong SST-gradient, the air-sea temperature and humidity differences in the warm sector result in negative (downward) surface sensible and latent heat fluxes (Figure 5a), both contributing toward cooling of the atmosphere. Cooling of the atmospheric boundary layer in the moisture loaded warm sector results in saturation and thus formation of precipitation, hence these surface fluxes likely contribute to a drier boundary layer. Notice that latent heat release associated with condensation during the formation of precipitation potentially offsets the cooling. In addition to the drying due to the cooling, the negative surface latent heat flux also implies that as the warm moist air moves poleward, it is cut-off from local moisture supply due to lack of evaporation from the ocean, which occurs in this case poleward of SST = 292 K, roughly around 40°S or about 2,000 km away from the coastal zone of Antarctica. Hence the relatively dry lower part of the troposphere in the warm sector can be attributed to air-sea interactions, where the lack of moisture supply via surface evaporation and cooling both contribute to a relatively dry boundary layer, thereby enhancing the signature of an elevated maximum of moisture transport.

Neglecting moisture changes due to phase transitions, the local change in moisture can be described by the moisture flux convergence,

$$\frac{\partial q}{\partial t} = -\nabla \cdot (q\vec{u}) = -\vec{u} \cdot \nabla q - q\nabla \cdot \vec{u} \tag{1}$$

where q represents the specific humidity and $\bar{u}$ the velocity field. The moisture flux convergence is separated in contributions from moisture advection and moisture convergence (right hand side). Below the moisture transport maximum, roughly below the 292 K isentrope, that is, the location of the low-level jet, there is a local moisture increase both by horizontal moisture advection (not shown) and by moisture convergence (Figure 4). However, this moisture increase does not seem to counterbalance the moisture lack/loss induced by air-sea interactions, as the specific humidity maximum is located above this region. Local maxima of moisture convergence at low-levels are located just upstream of the intersection of the 292 K isentrope with the surface (around 40°S), and over the coastal region of Antarctica (Figure 4). Thus we find the strongest moisture convergence over the sub-tropical moisture source region and at the polar precipitation region, whereas moisture convergence in between is relatively moderate. These features, combined with the elongated structure of moisture transport, hint at long-range moisture transport between these two locations. Note that the moisture flux convergence pattern (not shown) is analogous to the moisture convergence, but in regions of strong horizontal moisture gradients it is enhanced with a similar magnitude by the moisture advection (not shown). However, peak values in moisture convergence (close to Antarctica and around 40 S) are not matched in magnitude by the moisture advection.

Vertically integrated values of moisture flux convergence (Figure 5b) are most prominent along the eastern side of the entire warm-sector, which can be attributed to the overall zonal displacement of the warm-sector (see Figures 2e and 2f). Despite the dominant meridional flow direction, the horizontal *gradients* in moisture content are much larger in the zonal direction resulting in relative large local changes in moisture content in the zonal direction, and thus enhanced (suppressed) moisture flux convergence on the eastern (western) side of the warm sector. Upon approaching the steep orography of East Antarctica this pattern is disturbed, and local convergence due to interaction with the topography results in a broad region of strong moisture flux convergence which enhanced the local precipitation. Notice that upon reaching the Antarctic coastal region the atmosphere is much drier compared to lower latitudes (see Figure 3), thus similar values of moisture flux convergence are likely driven by strong local mass convergence.

3.2.2. Secondary Cyclogenesis

Prior to and during the precipitation event the large-scale atmospheric configuration acts as a wave-guide for short-wave upper-level disturbances. If the conditions in the troposphere are favorable for cyclone development, these upper-level disturbances result in cyclogenesis. As the main synoptic-scale cyclone starts to decay (around 15 February 12:00 UTC), the band of strong IVT associated with the first precipitation peak, ceases to reach Antarctica, though large values of IVT remain further North (Figure 6). At the same time, a small-scale upper-level disturbance, as evident from the wavy structure in the 2PVU isoline at 315 K (Figure 6a), approaches the region of remnants of high moisture content, initiating cyclogenesis along the western edge of the high-pressure system, just south of the main SST gradient. Coupling between a surface and upper-level cyclonic feature, which are slightly tilted toward each other, enforces cyclogenesis, akin to classical baroclinic development (Charney, 1948; Eady, 1949). The tilted direction is with respect to the baroclinic zone along the eastern side of the main cyclone (L_1), which is in this case meridionally orientated (Figure 6 and Figure S2). The deepening and propagation speed of the secondary cyclone (labeled L_{S3}, Figure 6) is remarkable, within 1 day it translates about 2,000 km and decreases ≈ 30 hPa in surface pressure. These features are likely a combined effect of coupling with the poleward intense upper-level jet associated with the trough, and the abundance of available moisture aiding rapid cyclogenesis via latent heat release. Notice that also this cyclone exhibits negative surface sensible and latent heat fluxes in the warm sector (Figure 7a). The effect of the secondary cyclone is strong moisture flux convergence *ahead* of the cyclone (L_{S3}, relative to the direction of propagation), thereby facilitating the transport of moisture toward East Antarctica (Figure 7b). The landfall of this secondary cyclone corresponds to the onset of the second precipitation maximum (16 February 09:00, see also Figure 1a).

In summary, we identified two distinctly different mechanisms that contributed to the long-range moisture transport: on synoptic scales, transport was dominated by isentropic up-gliding in the warm-sector of a large scale cyclone, whereas on sub-synoptic scales the rapid intensification and propagation of mesoscale cyclones contributed to poleward transport of moisture. Yet, in both cases, local moisture uptake along the poleward moisture transport is limited, highlighting the prominent role of air-sea temperature differences and resulting humidity gradients above the water during such events. Moisture uptake is only possible in
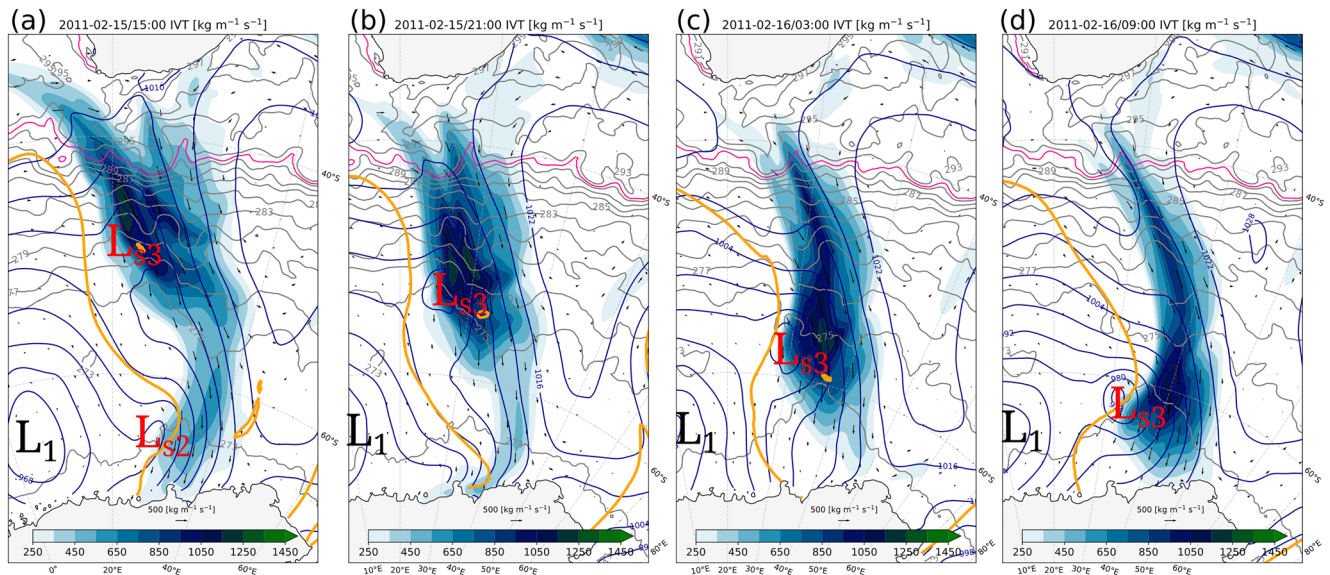
Figure 6. Overview of the temporal evolution prior to the second precipitation onset (every 6 h, timestamps in UTC as per title) showing vertically integrated vapor transport (shading and arrows, units: kg m^{-1} s^{-1}), sea level pressure (blue lines, units: hPa), sea surface temperature (gray lines, units: K, pink line: SST = 292 K). The upper level configuration is depicted by the orange line representing 2PVU at 315 K. The main cyclone is labeled L$_1$, and secondary cyclones are labeled L$_{S2}$ and L$_{S3}$. SST, sea surface temperature.
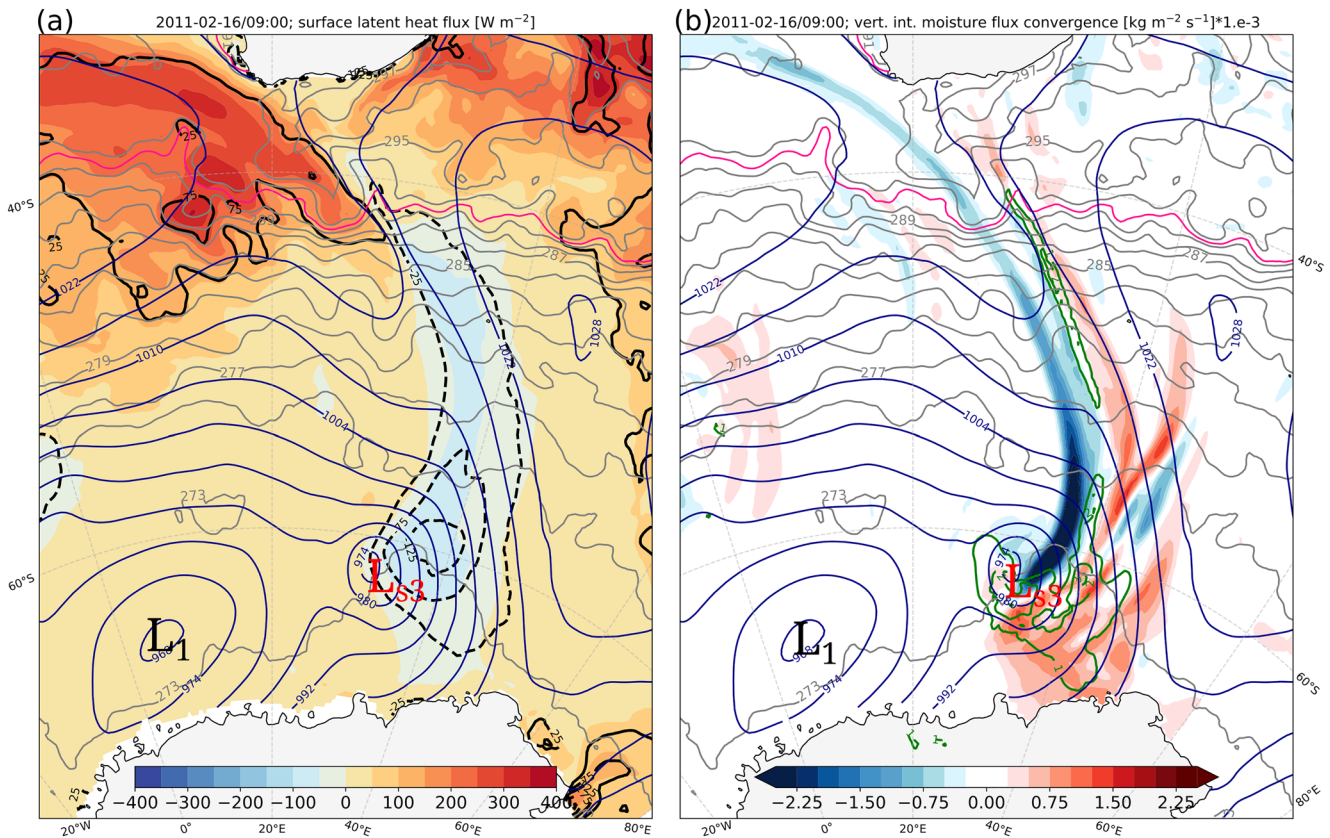
Figure 7. (a) Surface latent heat flux (shading, units: W m^{-2}) and surface sensible heat flux (black lines, negative dashed (downward), units: W m^{-2}). (b) Vertically integrated moisture flux convergence (shading, units: kg m^{-2} s^{-1}) and total precipitation (green, contour interval: 1 mm). Sea-level pressure (blue lines, units: hPa) and sea surface temperature (gray lines, units: K, pink-line: SST = 292 K). The main cyclone is labeled L$_1$, and the secondary cyclone L$_{S3}$. SST, sea surface temperature.
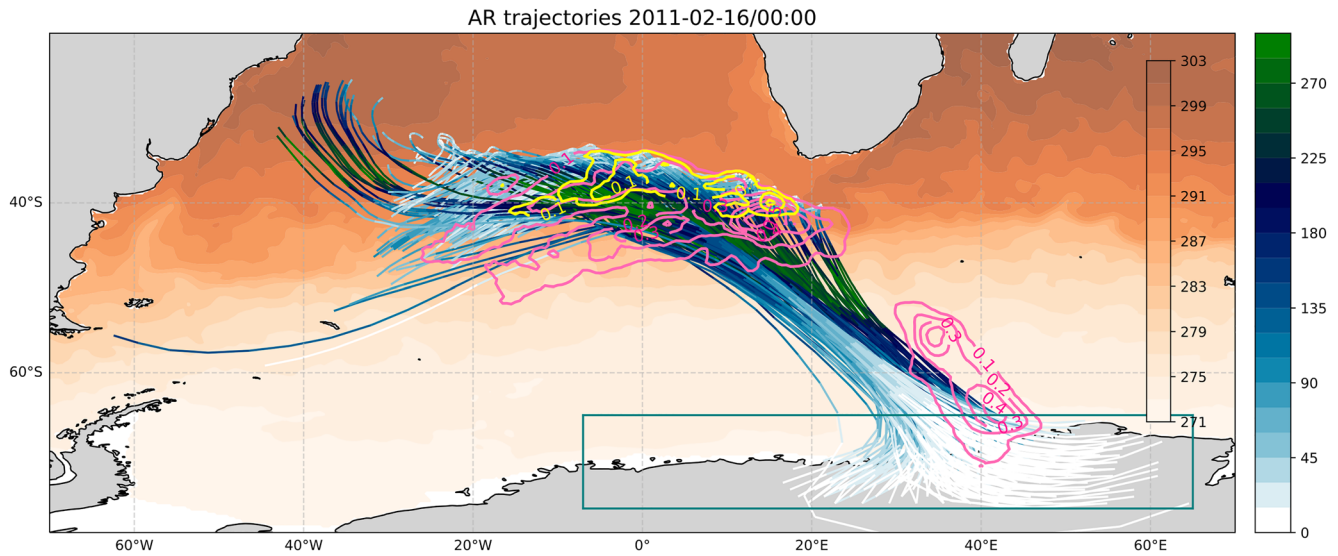
Figure 8. Kinematic backward trajectories (5 days) arriving on February 16, 2011 00:00 UTC (approximately during first peak in precipitation) over land in the region indicated by the box (which envelops the region of precipitation during the entire event) and exhibiting strong moisture transport (>250 g kg m^{-1}) sometime along their track. Trajectories are shaded by moisture transport (units: g kg m s^{-1}), the background shading shows the sea-surface temperature (units: K). Moisture uptake in the boundary layer (units: mm 3 h^{-1}) associated with precipitation inside the box on February 16, 2011, 00:00 UTC for all trajectories (pink lines) and for the selected trajectories (yellow lines).

regions with a conducive air-sea temperature difference, which in this case was several thousand kilometers away from the precipitation region, with limited surface evaporation between 40 and 60°S.

3.3. Lagrangian Perspective

In the previous section we used snapshots of the atmosphere, with a spatial extent of several thousand kilometers, to evaluate the atmospheric state prior to and during the precipitation event. In this section we will use a complementary approach by back-tracking the temporal evolution of air parcels from the continental precipitation region. We use our collection of backward trajectories to evaluate the evolution of an air-stream linking the sub-tropics and Antarctic continent, and pinpoint the spatial and temporal characteristics of the oceanic moisture sources that contributed to Antarctic precipitation.

#### 3.3.1. Coherent Air-Stream Linking Sub-Tropics to Antarctic

Figure 8 displays 5-day backward trajectories for air parcels arriving on February 16, 2011 00:00UTC, that is, during the first peak in precipitation, over the East Antarctic precipitation region and that exhibited a moisture flux >250 g kg^{-1} m s^{-1} at sometime along the trajectory. These air parcels exhibit high values of moisture flux sometime along their track, and could be designated as part of an atmospheric river. The selected trajectories follow a similar pathway for several days, and as such belong to a coherent air-stream located in the warm sector of the synoptic-scale cyclone (L_1). Besides a few outliers, the air parcels are located on the warmer side of the sea-surface temperature gradient, that is, roughly equatorward of the SST = 292 K isoline, 5 days before landfall. The surface moisture source region (see Section 2), associated with the selected trajectories, is located in the region around 40°S (yellow lines, Figure 8). The total moisture uptake in the boundary layer, established from all trajectories (pink lines, Figure 8) exhibits two distinct regions, one located in the sub-tropics (around 40°S) and another closer to the continent. The selected trajectories illustrate a pathway of long-range moisture transport from the sub-tropical moisture source region toward East-Antarctica. Notice however that they only account for a fraction of the total precipitation (14%) as only trajectories with high moisture flux are included. Reducing the selection threshold to 200 (150) g kg^{-1} m s^{-1} accounts for 29 (47) % of the total precipitation, with all moisture uptake taking place in the sub-tropical moisture source region. Thus, a rather coherent air-stream plays a prominent role in the poleward moisture transport by linking the sub-tropical moisture source region to the Antarctic precipitation region, while exhibiting high moisture fluxes.
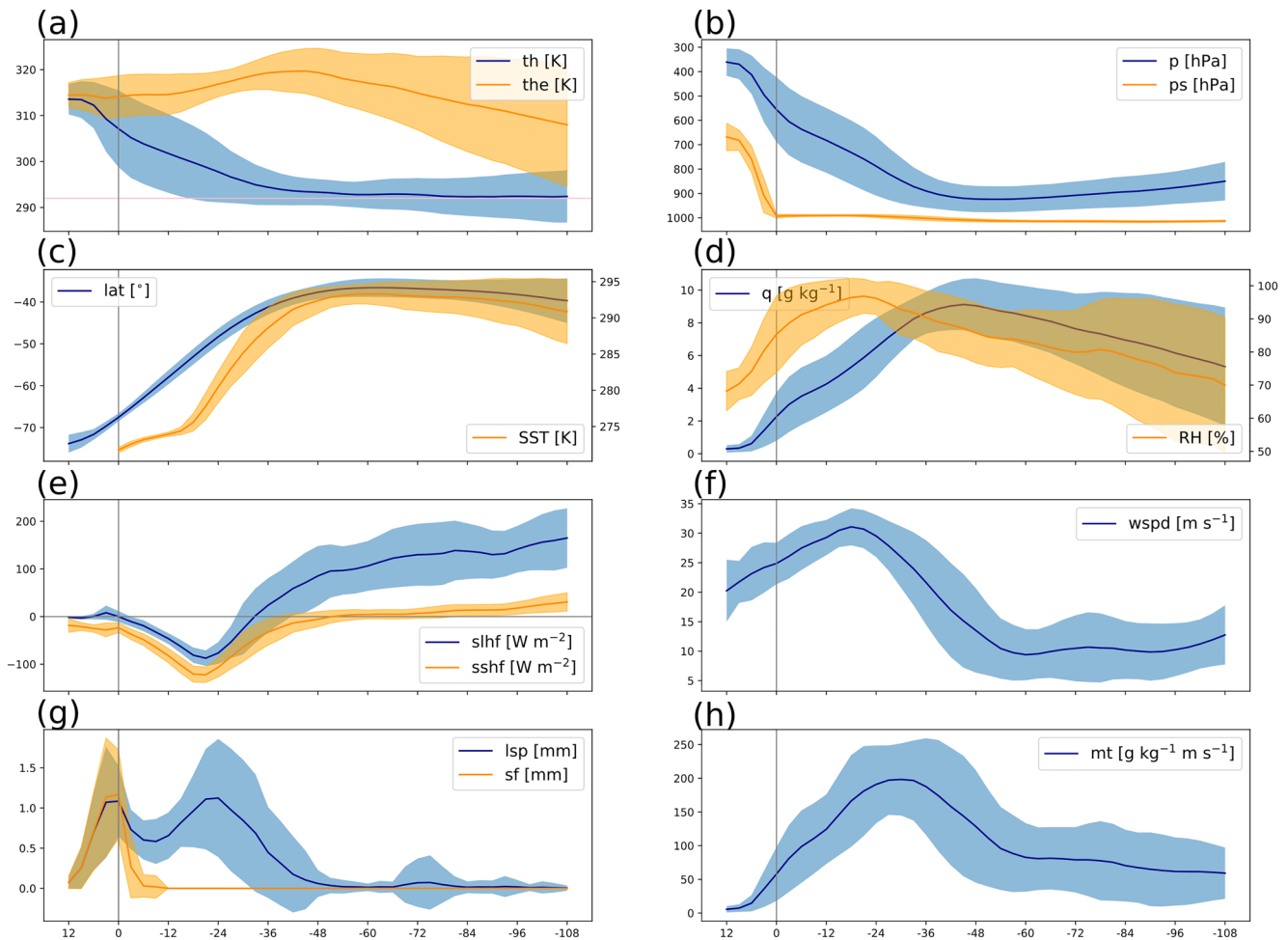
Figure 9. Properties along selected backward trajectories (see Figure 8 for selection details) showing mean values (lines) and standard deviation (shading). Values on x-axis indicate hours, data is plotted such that $t = 0$ h corresponds to landfall. The values of the surface fluxes are time-mean values for the previous hour, and precipitation comprised accumulated values over the previous hour, both wrt. the trajectory-timestamp. Abbreviations: th = potential temperature, the = equivalent potential temperature, ps = surface pressure, p = pressure, SST = sea surface temperature, lat = latitude, q = specific humidity, RH = relative humidity, sshf = surface sensible heat flux, slhf = surface latent heat flux, wspd = windspeed, lsp = large scale precipitation, sf = snowfall (convective + stratiform) and mt = moisture transport.

Figure 9 displays properties along the selected backward trajectories, that is, along trajectories exhibiting a moisture flux >250 g kg^{-1} m s^{-1} sometime prior to landfall. Up to approximately 2 days ($t = -48$ h) before landfall the selected air parcels reside at low-levels (between 950 and 800 hPa, Figure 9b), steadily gaining moisture (Figure 9d). During this period, their potential temperature remains rather constant and roughly equals the underlying SST (Figures 9a and 9c), resulting in negligible surface sensible heat fluxes (Figure 9e). During this phase, surface evaporation provides moisture input which increased the parcels' specific humidity (Figure 9d and 9e), resulting in a steady increase in relative humidity (Figure 9d). Roughly 48 h before landfall these air-parcels are "gathered" by the warm sector of the synoptic scale cyclone (L$_1$), and leave the sub-tropics on a poleward journey (Figure 9c). At this point, the air-parcels start to experience increases in wind speed while being lifted (Figures 9b and 9f). As the moisture loaded air-parcels ascent (starting at $t = -48$ h), saturation occurs due to adiabatic cooling, resulting in precipitation (Figure 9g), while the associated condensation resulting in increased potential temperature (Figure 9a). The slow rates of ascent and resolved precipitation indicate that the ascent is driven by isentropic up-gliding, as opposed to convectively forced ascent. As the air parcels ascent and move poleward, the underlying SST decreases (Figure 9c), and the air mass underneath is experiencing negative surface sensible and latent heat fluxes (Figures 9d and 9e), corroborating the lack of moisture input from surface evaporation and cooling by surface sensible heat fluxes that has been pointed out previously (see Section 3.2). Notice that the air parcels themselves are lifted
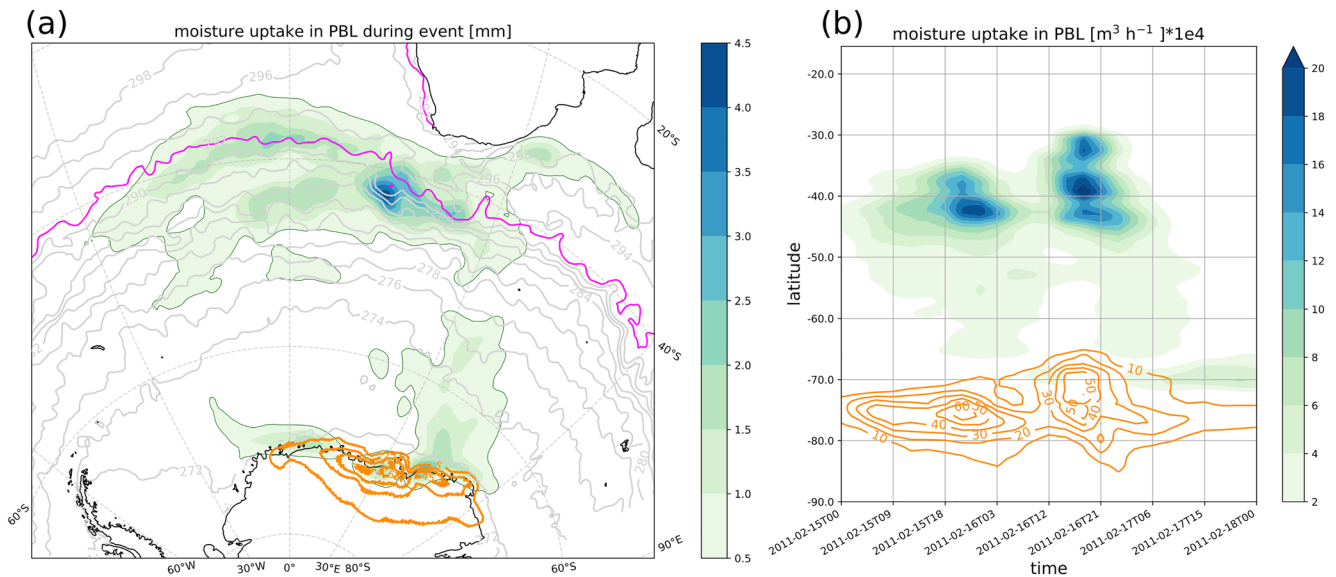
Figure 10. (a) Moisture uptake in the boundary layer during the event (15–18 February 2011, shading, units: mm), associated estimated precipitation (orange lines, contour interval: 20 mm), and sea surface temperature (mean during the event, gray lines, units: K, pink-line: SST = 292 K). (b) Hovmöller diagram (time-latitude) displaying moisture uptake in boundary layer integrated per latitude band (shading, units: $m^3\ h^{-1}$) and corresponding precipitation (orange lines, units: $m^3\ h^{-1}$). The moisture uptake regions and precipitation are based on backward trajectories.

and thus moving away from the surface. While the parcels are lifted the wind speed increases, accompanied by an increase in moisture transport (Figures 9f and 9h). Around $t = -30$ h the moisture transport peaks whereafter it steeply declines as precipitation depletes the air parcels' moisture content. Upon approaching the coastal regions the air-parcels are cooled to subfreezing temperatures (around $t = -15$ h, not shown) after which the dominant precipitation type changes from rain to snowfall (Figure 9g). Note that the air-parcels nearly lost all their moisture at this point, with the final enhanced ascent due to the steep orography over the continent resulting in a localized peak in snowfall (Figures 9b and 9g).

Overall the development of the coherent air-stream is in agreement with the Eulerian description in Section 3.2, in which a warm-conveyor belt like feature is bridging the gap between the sub-tropical moisture source region and Antarctic precipitation. In addition to the Eulerian perspective, the trajectory analysis confirmed limited surface evaporation and downward surface sensible heat fluxes along the poleward journey, underscoring the notion of long-distance moisture transport prior to and during the precipitation event. The role of WCB like moisture transport during ARs was previously observed by Sodemann and Stohl (2013), similarly Komatsu et al. (2018) associated slantwise ascent with intense poleward moisture transport in the Arctic.

3.3.2. Moisture Sources

Using the methodology of Sodemann et al. (2008); Sodemann (2020) (see also Section 2) we account for moisture changes along all backward trajectories that arrived at the precipitation area during the event to identify the most likely moisture uptake region. The magnitude and spatial distribution of the estimated precipitation from this methodology is largely in agreement with the precipitation output from ERA5 (compare Figures 1b and 10a), albeit ERA5 precipitation exhibits more localized peak values. This correspondence provides confidence in the ability of this methodology to represent the changes in moisture along the backward trajectories.

During the event the primary moisture uptake via surface evaporation is over a several 100 km wide band centered around 40°S, about 2,000 km equator ward of the precipitation region (Figure 10a). This subtropical region accounts for the bulk of the surface moisture uptake, with 2/3 of the total surface moisture uptake during the event taking place equator ward of 50°S and more than a quarter (28%) equatorward of 40°S. A secondary moisture source region is located near the coast of East Antarctica. With only 16% of the surface moisture uptake taking place south of 60°S, moisture uptake in this secondary region contributes

little to the precipitation during the event. Furthermore, contributions to the precipitation from moisture sources in the vicinity of Antarctica occur predominantly toward the end of the event, that is, after the second precipitation peak. Note that the surface moisture uptake in Figure 10b is derived from backward trajectories associated with the estimated precipitation for each timestamp, hence the moisture uptake takes place *before* the plotted timestamp. The mean and standard deviation of the transport distance between the source region and precipitation region is 5,578 ± 533 km with a transport duration of 4.2 ± 0.3 days. This roughly equates to transport velocities around 15 m s^{-1}. These somewhat high velocities are in agreement with the strong moisture transport along the poleward part of the coherent air-stream (see Section 3.3.1), and also with the rapidly propagating secondary cyclones (see Section 3.2.2). The large gap between the major uptake region and precipitation region confirms that the warm air mass that facilitated the moisture transport, as described in the previous sections, indeed experienced limited moisture uptake from surface evaporation during the poleward moisture transport. Furthermore, the Hövemuller diagram, showing the precipitation and moisture uptake as derived from backward trajectories (Figure 10b) clearly shows the two distinctive phases of the event. The concurrent occurrence of the two peaks in Antarctic precipitation and sub-tropical moisture uptake, indicate that both the synoptic and mesoscale cyclogenesis contributed to long-range moisture transport. In addition, it corroborates the previously pointed out (Section 3.2 and 3.3) limited local surface evaporation along the region of poleward moisture transport.

Besides the importance of the atmospheric configuration during the precipitation event, there is some evidence that the distribution of the SST contributed to the pre-conditioning, that is, the high atmospheric moisture load prior to the poleward moisture transport. The local maximum of moisture uptake (south of the African coast) is roughly collocated with poleward excursion of warmer SSTs (see SST = 292 K, pink line, Figure 10a and Figure S3) during the event. This localized poleward excursion of warmer SSTs is located in the Agulhas current leakage region, a region with frequent shedding of ocean surface eddies from the Agulhas current into the South Atlantic ocean (Durgadoo et al., 2017). Furthermore, the moisture uptake region at 40°S experienced climatological (with respect to 2006–2016 monthly mean) anomalously warm SSTs (see Figure S3), providing another indicator of the potential importance of the sub-tropical SST distribution for extreme precipitation events over the Antarctic continent.

4. Summary and Conclusions

4.1. Summary

We provide a detailed analysis of the moisture transport and sources that contributed to an extreme precipitation event over East Antarctica. Coastal precipitation during the event exhibited sustained extreme precipitation rates for several days. The temporal evolution of the coastal precipitation comprised two phases of enhanced precipitation rates, both contributing roughly equally to the total precipitation during the event. A comparison of precipitation fields from ERA5 and local precipitation observations at Princess Elisabeth showed a good temporal agreement indicating that the event is reasonably well represented in ERA5.

The planetary-scale atmospheric configuration during the event consisted of a blocking situation which introduced a sustained meridional flow direction from the sub-tropics to the Antarctic continent. Along this meridional flow, synoptic-scale cyclogenesis provided a warm-conveyor belt alike isentropic up-gliding of moisture loaded air parcels. As the warm moist air started to progress poleward, the air-sea temperature differences reversed due to decreasing SSTs. As a consequence, the underlying air mass experienced negative (downward) surface sensible and latent heat fluxes, effectively providing a cut-off from surface evaporation, and inducing cooling of the lower troposphere during the poleward moisture transport. Landfall of the moisture loaded warm sector in East Antarctica corresponded to the onset of enhanced precipitation over the coastal region. The established warm moist corridor provided favorable conditions for secondary cyclogenesis, which was initiated by transient short-waves along the meridionally orientated upper-level jet. The mesoscale cyclone had a remarkable deepening rate and propagation speed, likely attributable to the coupling with the upper levels and the abundance of available moisture at low levels aiding cyclogenesis via latent heat release. This mesoscale cyclone induced strong moisture flux convergence ahead of the cyclone, and landfall of this region corresponded to a second enhancement of coastal precipitation. Evaluation of the moisture source regions by accounting for moisture changes in traced air parcels confirmed the limited

surface evaporation between the oceanic moisture source and continental precipitation during the event, with the primary moisture source region located in the sub-tropics.

4.2. Concluding Remarks

The elongated structure of high IVT values associated with this case study was previously labeled as an AR (Gorodetskaya et al., 2014), and would be classified as such by most AR feature detection algorithms (see Rutz et al., 2019 and references therein). Yet, the detection of AR-features provides only limited insight in the associated processes. In this case study, initially the elongated region of high IVT values was predominantly attributable to slantwise ascent of moisture loaded air parcels, whereas at later stages the rapid propagation of a mesoscale cyclone contributed to the collocation of moisture and strong wind speeds. The development of mesoscale features is not uncommon during ARs. For example, the AR-case investigated by Ralph et al. (2010) was accompanied by a frontal-wave which contributed to heavy precipitation, and also Luo and Tung (2015) concluded that embedded mesoscale convective systems played a significant role in the moisture transport during two AR-cases. Moreover, a study by Sinclair and Dacre (2018) points to the relevance of mesoscale cyclones for poleward moisture transport. They showed that among extratropical cyclones, rapidly propagating open frontal-waves, resembling secondary cyclones, exhibited the strongest poleward moisture fluxes in the Southern Hemisphere. Embedded mesoscale features and the interplay between different scales highlights the complex nature of AR-signatures, pinpointing the need for future investigation on the role of mesoscale features and scale interactions during ARs.

Our analysis, that is, Eulerian snapshots of the atmosphere, the Lagrangian airstream exhibiting AR-characteristics, and identification of the most likely moisture source region, indicate that the case described here exhibited long-range moisture transport from the sub-tropics to the Antarctic continent. This is in contrast to case studies in the Northern Hemisphere (e.g., Bao et al., 2006; Cordeira et al., 2013; Ralph et al., 2010; Sodemann & Stohl, 2013), in which only a fraction of the moisture is transported along the entire AR length. In these case studies the AR moisture sources are, besides a (sub)tropical source, attributed to horizontal moisture convergence along the AR-structure and local surface evaporation. Furthermore, AR-signatures in the North Atlantic seems to be maintained by a continuous process of local surface evaporation and precipitation (Dacre et al., 2015), whereas in the case presented here this mechanism was absent due to a lack of surface evaporation. Overall our case study shows that the underlying dynamical pathways for AR-signatures cover a broad spectrum of mechanisms, and include distinct hemispheric differences which are likely introduced by the distribution of SSTs.

While we did not perform a climatology of extreme precipitation events over East Antarctica, other climatological research provides some context for individual case studies. There are several indicators that the case studied here is rather representative for ice-sheet accumulation events over Antarctica coastal regions. As pointed out by Turner et al. (2019), climatologically extreme precipitation events contribute to 50%–70% of coastal precipitation in Antarctica. Furthermore, the Lagrangian analysis by Sodemann and Stohl (2009) indicated that climatologically moisture source regions related to Antarctic precipitation exhibit a maximum around 40°S at similar longitudes. In addition, Sinclair and Dacre (2018) found that from their collection of extra-tropical cyclones the strongest poleward moisture transport occurred in fast propagating frontal-wave cyclones, akin to our rapidly propagating mesoscale cyclone. As our case study features typical climatological conditions for coastal Antarctic precipitation, including sustained extreme precipitation, a sub-tropical moisture source and rapidly propagating open-wave cyclones, it seems reasonable that other features, most prominently the limited surface evaporation during long-range moisture transport, is also typical for such events.

Sustained periods of significant precipitation over the coastal region of Antarctica requires poleward excursions of warm moist air masses to account for a sufficient moisture load. Yet, as the underlying SSTs decrease poleward, such events will be cut-off from surface evaporation, hence almost by default extreme precipitation events over coastal Antarctica depend on long-range moisture transport. This also implies that, as the moisture is loaded to the atmosphere in the sub-tropics, the conditions in this region, in particular the SST distribution, produce an imprint on Antarctic precipitation. Based on the similarities of our case study with typical climatological conditions and the above reasoning, we hypothesize that also in a climatological framework the distribution of sub-tropical SSTs are linked to coastal precipitation over Antarctica.

This in turn affects ice-sheet accumulation, with shifts in the Southern Ocean SST-gradients or local SST anomalies in the sub-tropics conceivably modulating the Antarctic ice-sheet growth, which potentially has implications for climate interpretation from such sources.

Data Availability Statement

Data for this study is provided by the European Center for Medium-Range Weather Forecasts (ECMWF) and is available via the Copernicus Climate Change Service Climate Data Store (https://cds.climate.co-pernicus.eu/cdsapp). The Belgian Science Policy Office (BELSPO; projects BR/143/A2/AEROCLOUD and HYDRANT EA/01/04AB) supported observations at Princess Elisabeth Station, the observational data set is accessible via https://ees.kuleuven.be/hydrant/aerocloud/.

References

Aemisegger, F., & Papritz, L. (2018). A climatology of strong large-scale ocean evaporation events. Part I: Identification, global distribution, and associated climate conditions. *Journal of Climate*, *31*(18), 7287–7312. https://doi.org/10.1175/JCLI-D-17-0591.1

Andrew, S., Ivins, E., Rignot, E., Smith, B., van den Broeke, M., Velicogna, I., et al. (2018). Mass balance of the Antarctic Ice Sheet from 1992 to 2017. *Nature*, *558*, 219–222.

Bao, J.-W., Michelson, S. A., Neiman, P. J., Ralph, F. M., & Wilczak, J. M. (2006). Interpretation of enhanced integrated water vapor bands associated with extratropical cyclones: Their formation and connection to tropical moisture. *Monthly Weather Review*, *134*, 1063–1080. https://doi.org/10.1175/mwr3123.1

Boening, C., Lebsock, M., Landerer, F., & Stephens, G. (2012). Snowfall-driven mass change on the East Antarctic ice sheet. *Geophysical Research Letters*, *39*(21). https://doi.org/10.1029/2012GL053316

Booth, J. F., Dunn-Sigouin, E., & Pfahl, S. (2017). The relationship between extratropical cyclone steering and blocking along the North American East Coast. *Geophysical Research Letters*, *44*(23), 11–976. https://doi.org/10.1002/2017gl075941

Bromwich, D. H. (1988). Snowfall in high Southern latitudes. *Reviews of Geophysics*, *26*(1), 149–168. https://doi.org/10.1029/rg026i001p00149

Charney, J. (1948). On the scale of atmospheric motions. *Geophysical Publications Oslo*, *17*, 3–17.

Cordeira, J. M., Ralph, F. M., & Moore, B. J. (2013). The development and evolution of two atmospheric rivers in proximity to Western North Pacific tropical cyclones in October 2010. *Monthly Weather Review*, *141*(12), 4234–4255. https://doi.org/10.1175/MWR-D-13-00019.1

Dacre, H. F., Clark, P. A., Martinez-Alvarado, O., Stringer, M. A., & Lavers, D. A. (2015). How do atmospheric rivers form? *Bulletin of the American Meteorolgical Society*, *96*(8), 1243–1255. https://doi.org/10.1175/BAMS-D-14-00031.1

Drumond, A., Taboada, E., Nieto, R., Gimeno, L., Vicente-Serrano, S. M., & López-Moreno, J. I. (2016). A Lagrangian analysis of the present-day sources of moisture for major ice-core sites. *Earth System Dynamics*, *7*, 549–558. https://doi.org/10.5194/esd-7-549-2016

Durgadoo, J. V., Rühs, S., Biastoch, A., & Böning, C. W. B. (2017). Indian Ocean sources of Agulhas leakage. *Journal of Geophysical Research: Oceans*, *122*(4), 3481–3499. https://doi.org/10.1002/2016JC0122676

Eady, E. T. (1949). Long waves and cyclone waves. *Tellus*, *1*, 33–52. https://doi.org/10.3402/tellusa.v1i3.8507

Gimeno, L., Dominguez, F., Nieto, R., Trigo, R., Drumond, A., Reason, C. J. C., et al. (2016). Major mechanisms of atmospheric moisture transport and their role in extreme precipitation events. *Annual Review of Environment and Resources*, *41*, 117–141. https://doi.org/10.1146/annurev-environ-110615-085558

Gorodetskaya, I. V., Kneifel, S., Maahn, M., Van Tricht, K., Thiery, W., Schween, J. H., et al. (2015). Cloud and precipitation properties from ground-based remote-sensing instruments in east Antarctica. *The Cryosphere*, *9*, 285–304. https://doi.org/10.5194/tc-9-285-2015

Gorodetskaya, I. V., Tsukernik, M., Claes, K., Ralph, M. F., Neff, W. D., & van Lipzig, N. P. M. (2014). The role of atmospheric rivers in anomalous snow accumulation in East Antarctica. *Geophysical Research Letters*, *41*(17), 6199–6206. https://doi.org/10.1002/2014GL060881

Grazioli, J., Genthon, C., Boudevillain, B., Duran-Alarcon, C., Del Guasta, M., Madeleine, J.-B., & Berne, A. (2017). Measurements of precipitation in Dumont d'Urville, Adélie Land, East Antarctica. *The Cryosphere*, *11*, 1797–1811. https://doi.org/10.5194/tc-11-1797-2017

Hersbach, H., Bell, B., Berrisford, P., Hirahara, S., Horányi, A., Muñoz-Sabater, J., et al. (2020). The ERA5 global reanalysis. *Quarterly Journal of the Royal Meteorological Society*, *146*, 1999–2049. https://doi.org/10.1002/qj.3803

Hewson, T. D. (1998). Objective fronts. *Meteorological Applications*, *5*, 37–65. https://doi.org/10.1017/s1350482798000553

Hirasawa, N., Nakamura, H., Motoyama, H., Hayashi, M., & Yamanouchi, T. (2013). The role of synoptic-scale features and advection in prolonged warming and generation of different forms of precipitation at Dome Fuji station, Antarctica, following a prominent blocking event. *Journal of Geophysical Research: Atmospheres*, *118*(13), 6916–6928. https://doi.org/10.1002/jgrd.50532

Jenkner, E., Leive, A., Schwenk, I., Schwierz, C., Dierer, S., & Leuenberger, D. (2010). Health care spending issues in advanced economies. *Meteorological Applications*, *2010*, 1–18. https://doi.org/10.5089/9781462369713.005

King, M. A., Bingham, R. J., Moore, P., Whitehouse, P. L., Bentley, M. J., & Milne, G. A. (2012). Lower satellite-gravimetry estimates of Antarctic sea-level contribution. *Nature*, *491*(7425), 586–589. https://doi.org/10.1038/nature11621

Komatsu, K. K., Alexeev, V. A., Repina, I. A., & Tachibana, Y. (2018). Poleward upgliding Siberian atmospheric rivers over sea ice heat up Arctic upper air. *Scientific Reports*, *8*. https://doi.org/10.1038/s41598-018-21159-6

Kulie, M. S., & Bennartz, R. (2009). Utilizing spaceborne radars to retrieve dry snowfall. *Journal of Applied Meteorology and Climatology*, *48*(12), 2564–2580. https://doi.org/10.1175/2009JAMC2193.1

Kurita, N., Hirasawa, N., Koga, S., Matsushita, J., Steen-Larsen, H. C., Masson-Delmotte, V., & Fujiyoshi, Y. (2016). Influence of large-scale atmospheric circulation on marine air intrusion toward the East Antarctic coast. *Geophysical Research Letters*, *43*(17), 9298–9305. https://doi.org/10.1002/2016gl070246

Landais, A., Casado, M., Prié, F., Magand, O., Arnaud, L., Ekaykin, A., et al. (2017). Surface studies of water isotopes in Antarctica for quantitative interpretation of deep ice core data. *Comptes Rendus Geoscience*, *349*, 139–150. https://doi.org/10.1016/j.crte.2017.05.003

Lenaerts, J. T. M., van Meijgaard, E., van den Broeke, M. R., Ligtenberg, S. R. M., Horwath, M., & Isaksson, E. (2013). Recent snowfall anomalies in Dronning Maud Land, East Antarctica, in a historical and future climate perspective. *Geophysical Research Letters*, *40*(11), 2684–2688. https://doi.org/10.1002/grl.50559

Luo, Q., & Tung, W.-w. (2015). Case study of moisture and heat budgets within atmospheric rivers. *Monthly Weather Review*, *143*(10), 4145–4162. https://doi.org/10.1175/MWR-D-15-0006.1

Maahn, M., & Kollias, P. (2012). Improved micro rain radar snow measurements using Doppler spectra post-processing. *Atmospheric Measurement Techniques*, *5*(11), 2661–2673. https://doi.org/10.5194/amt-5-2661-2012

Madonna, E., Wernli, H., Joos, H., & Martius, O. (2014). Warm conveyor belts in the ERA-Interim Dataset (1979-2010). Part I: Climatology and potential vorticity evolution. *Journal of Climate*, *27*(1), 3–26. https://doi.org/10.1175/JCLI-D-12-00720.1

Matrosov, S. Y. (2007). Modeling backscatter properties of snowfall at millimeter wavelengths. *Journal of the Atmospheric Sciences*, *64*(5), 1727–1736. https://doi.org/10.1175/JAS3904.1

Mendes, M. C. D., Trigo, R. M., Cavalcanti, I. F. A., & DaCamara, C. C. (2008). Blocking episodes in the Southern Hemisphere: Impact on the climate of adjacent continental areas. *Pure and Applied Geophysics*, *165*(9–10), 1941–1962. https://doi.org/10.1007/s00024-008-0409-4

Papritz, L., Pfahl, S., Rudeva, I., Simmonds, I., Sodemann, H., & Wernli, H. (2014). The role of extratropical cyclones and fronts for Southern Ocean freshwater fluxes. *Journal of Climate*, *27*(16), 6205–6224. https://doi.org/10.1175/JCLI-D-13-00409.1

Ralph, F. M., Neiman, P. J., Kiladis, G. N., Weickmann, K., & Reynolds, D. W. (2011). A multiscale observational case study of a Pacific Atmospheric river exhibiting tropical-extratropical connections and a mesoscale frontal wave. *Monthly Weather Review*, *139*, 1169–1189. https://doi.org/10.1175/2010MWR3596.1

Rignot, E., Mouginot, J., Scheuchl, B., van den Broeke, M., van Wessem, M. J., & Morlighem, M. (2019). Four decades of Antarctic Ice Sheet mass balance from 1979-2017. *Proceedings of the National Academy of Sciences of the United States of America*, *116*(4), 1095–1103. https://doi.org/10.1073/pnas.1812883116

Rutz, J. J., Shields, C. A., Lora, J. M., Payne, A. E., Guan, B., Ullrich, P., et al. (2019). The atmospheric river tracking method intercomparison project (ARTMIP): quantifying uncertainties in atmospheric river climatology. *Journal of Geophysical Research - D: Atmospheres*, *124*(13), 13777–13802. https://doi.org/10.1029/2019JD030936

Schlosser, E., Dittmann, A., Stenni, B., Powers, J. G., Manning, K. W., Masson-Delmotte, V., et al. (2017). The influence of the synoptic regime on stable water isotopes in precipitation at dome c, east Antarctica. *The Cryosphere*, *11*, 2345–2361. https://doi.org/10.5194/tc-11-2345-2017

Schlosser, E., Manning, K. W., Powers, J. G., Duda, M. G., Birnbaum, G., & Fujita, K. (2010). Characteristics of high-precipitation events in Dronning Maud Land, Antarctica. *Journal of Geophysical Research*, *115*(D14). https://doi.org/10.1029/2009JD013410

Shepard, A., Ivins, E. R., Geruo, A., Barletta, V. R., Bentley, M. J., Bettadpur, S., et al. (2012). A reconciled estimate of ice-sheet mass balance. *Science*, *338*(6111), 1183–1189.

Sinclair, V. A., & Dacre, H. (2018). Which extratropical cyclones contribute most to the transport of moisture in the Southern Hemisphere? *Journal of Geophysical Research: Atmospheres*, *124*(5), 2525–2545.

Sodemann, H. (2020). Beyond turnover time: Constraining the lifetime distribution of water vapor from simple and complex approaches. *Journal of the Atmospheric Sciences*, *77*(2), 413–433. https://doi.org/10.1175/JAS-D-18-036.110.1175/jas-d-18-0336.1

Sodemann, H., Schwierz, C., & Wernli, H. (2008). Inter-annual variability of Greenland winter precipitation sources: Lagrangian moisture diagnostic and North Atlantic Oscillation influence. *Journal of Geophysical Research*, *113*(D3). https://doi.org/10.1029/2007jd008503

Sodemann, H., & Stohl, A. (2009). Asymmetries in the moisture origin of Antarctic precipitation. *Geophysical Research Letters*, *36*(22). https://doi.org/10.1029/2009GL040242

Sodemann, H., & Stohl, A. (2013). Moisture origin and meridional transport in atmospheric rivers and their association with multiple cyclones*. *Monthly Weather Review*, *141*(8), 2850–2868. https://doi.org/10.1175/mwr-d-12-00256.1

Souverijns, N., Gossart, A., Gorodetskaya, I. V., Lhermitte, S., Mangold, A., Laffineur, Q., & van Lipzig, N. P. (2018). How does the ice sheet surface mass balance relate to snowfall? Insights from a ground-based precipitation radar in East Antarctica. *The Cryosphere*, *12*(6), 1983–2003. https://doi.org/10.5194/tc-12-1987-2018

Souverijns, N., Gossart, A., Lhermitte, S., Gorodetskaya, I. V., Kneifel, S., Maahn, M., et al. (2017). Estimating radar reflectivity—Snowfall rate relationships and their uncertainties over Antarctica by combining disdrometer and radar observations. *Atmospheric Research*, *196*, 211–223. https://doi.org/10.1016/j.atmosres.2017.06.001

Sprenger, M., & Wernli, H. (2015). The LAGRANTO Lagrangian analysis tool - version 2.0. *Geoscientific Model Development*, *8*, 2569–2586. https://doi.org/10.5194/gmd-8-2569-2015

Stenni, B., Scarchilli, C., Masson-Delmotte, V., Schlosser, E., Ciardini, V., Dreossi, G., et al. (2016). Three-year monitoring of stable isotopes of precipitation at Concordia station, east Antarctica. *The Cryosphere*, *10*, 2415–2428. https://doi.org/10.5194/tc-10-2415-2016

Tamarin, T., & Kaspi, Y. (2016). The poleward motion of extratropical cyclones from a potential vorticity tendency analysis. *Journal of the Atmospheric Sciences*, *73*(4), 1687–1707. https://doi.org/10.1175/jas-d-15-0168.1

Tietäväinen, H., & Vihma, T. (2008). Atmospheric moisture budget over Antarctica and the Southern Ocean based on the ERA-40 reanalysis. *International Journal of Climatology*, *28*(15), 1977–1995. https://doi.org/10.1002/joc.1684

Turner, J., Phillips, T., Thamban, M., Rahaman, W., Marshall, G. J., Wille, J. D., et al. (2019). The dominant role of extreme precipitation events in Antarctic snowfall variability. *Geophysical Research Letters*, *46*(6), 3502–3511. https://doi.org/10.1029/2018gl081517

Uotila, P., Vihma, T., & Tsukernik, M. (2013). Close interactions between the Antarctic cyclone budget and large-scale atmospheric circulation. *Geophysical Research Letters*, *40*(12), 3237–3241. https://doi.org/10.1002/grl.50560

Welker, C., Martius, O., Froidevaux, P., Reijmer, C. H., & Fischer, H. (2014). A climatological analysis of high-precipitation events in Dronning Maud Land, Antarctica, and associated large-scale atmospheric conditions. *Journal of Geophysical Research: Atmospheres*, *119*(21), 11–932. https://doi.org/10.1002/2014jd022259

Wille, J. D., Favier, V., Dufour, A., Gorodetskaya, I. V., Turner, J., Agosta, C., & Codron, F. (2019). West Antarctic surface melt triggered by atmospheric rivers. *Nature Geoscience*, *12*(11), 911–916. https://doi.org/10.1038/s41561-019-0460-1

Woolings, T., Barriopedro, D., Methven, J., Son, S.-W., Martius, O., Harvey, B., & Seneviratne, S. (2018). Blocking and its response to climate change. *Current Climate Change Reports*, *4*, 287–300. https://doi.org/10.1007/s40641-018-0108-z

Zhu, Y., & Newell, R. E. (1998). A proposed algorithm for moisture fluxes from atmospheric rivers. *Monthly Weather Review*, *126*, 725–735. https://doi.org/10.1175/1520-0493(1998)126<0725:apafmf>2.0.co;2